Article:

Qian, L, Burns, AG, Solomon, SS et al. (7 more authors) (2018) Temporal Variability of Atomic Hydrogen From the Mesopause to the Upper Thermosphere. Journal of Geophysical Research: Space Physics, 123 (1). pp. 1006-1017. ISSN 2169-9380

https://doi.org/10.1002/2017JA024998

Temporal Variability of Atomic Hydrogen From the Mesopause to the Upper Thermosphere

Liying Qian[1], Alan G. Burns[1], Stan S. Solomon[1], Anne K. Smith[2], Joseph McInerney[1], Linda Hunt[3], Daniel Marsh[1,2], Hanli Liu[1], Martin Mlynczak[3], Francis Vitt[1,2]

[1]High Altitude Observatory, National Center for Atmospheric Research, USA

[2]Atmospheric Chemistry Observations & Modeling Laboratory, National Center for Atmospheric Research, USA

[3]NASA Langley Research Center, Hampton, Virginia, USA

Submitted to Journal of Geophysical Research, 2017

Abstract. We investigate atomic hydrogen (H) variability from the mesopause to the upper thermosphere, on time scales of solar cycle, seasonal, and diurnal, using measurements made by the Sounding of the Atmosphere using Broadband Emission Radiometry (SABER) instrument on the Thermosphere Ionosphere Mesosphere Energetics Dynamics (TIMED) satellite, and simulations by the National Center for Atmospheric Research Whole Atmosphere Community Climate Model - eXtended (WACCM-X). In the mesopause region (85 to 95 km), the seasonal and solar cycle variations of H simulated by WACCM-X are consistent with those from SABER observations: H density is higher in summer than in winter, and slightly higher at solar minimum than at solar maximum. However, mesopause region H density from the Mass-Spectrometer-Incoherent-Scatter (NRLMSISE-00) empirical model has reversed seasonal variation compared to WACCMX and SABER. From the mesopause to the upper thermosphere, H density simulated by WACCM-X switches its solar cycle variation twice, and seasonal dependence once, and these changes of solar cycle and seasonal variability occur in the lower thermosphere (~ 95 to 130

km); whereas H from NRLMSISE-00 does not change solar cycle and seasonal dependence from the mesopause through the thermosphere. In the upper thermosphere (above 150 km), H density simulated by WACCM-X is higher at solar minimum than at solar maximum, higher in winter than in summer, and also higher during nighttime than daytime. The amplitudes of these variations are on the order of factors of ~10, ~2, and ~ 2, respectively. This is consistent with NRLMSISE-00.

1. Introduction

Atomic hydrogen (H) is one of the members of the odd hydrogen (HO_x) family (HO_x =H+OH+HO_2). The HO_x family members are produced in the atmosphere by dissociation of H_2O, H_2, and CH_4. At altitudes from the Earth's surface to about 80 km, the lifetime of the HO_x family is significantly shorter than the time scales of transport [Brasseur and Solomon, 2005]. In the mesopause region (~ 85 – 100 km), the lifetime of HO_x (> 1 day) becomes comparable to or larger than transport time scales and, therefore, transport effects are important. In the mesosphere, H participates in a highly exothermic reaction with ozone (O_3) that generates highly vibrationally excited hydroxyl (OH), which emits at the Meinel band (~2 µm). Measurement of this OH radiation enables the H density to be inferred by remote sensing [e.g., Thomas, 1990; Kaufmann et al., 2013; Mlynczak et al., 2014].

In the thermosphere (~ 100 – 600 km), atomic hydrogen becomes the dominant species of the HO_x family. H is a minor species in the thermosphere, but becomes increasingly important towards the upper thermosphere. Its concentration can be estimated by solving the hydrogen continuity equation, with contributions from horizontal and vertical advection, photochemical production and loss, eddy diffusion, and molecular diffusion. In the thermosphere, chemical production and loss are primarily the result of the following charge exchange reactions:

$$H^+ + \mathrm{O} \xrightarrow{k1} O^+ + H,\ O^+ + H \xrightarrow{k2} H^+ + \mathrm{O}$$

where k_1 and k_2 are temperature dependent chemical reaction rates. Another charge exchange reaction is between H and H^+, which can influence hydrogen kinetics and escape processes [Chamberlain and Hunten, 1987]. However, these changes due to charge exchange reactions have a relatively small effect on the total hydrogen budget in the thermosphere, compared with changes from dynamics.

Beyond the thermosphere, H becomes the dominant atmospheric constituent in the exosphere, where it scatters the sunlight at Lyman-α (1216 Å) and produces the luminous diffuse cloud known as the geocorona, extending out to several Earth radii. Ground-based observations of optical emissions, typically the faint H Balmer-α emission at 6563 Å, and space-based measurements of bright H Lyman-α emission at 1216 Å have been used to infer geocoronal H abundance [e.g., Anderson et al., 1987; Bush and Chakrabarti, 1995; Bishop et al., 2001; Qin and Waldrop, 2016; Qin et al., 2017]. In addition, charge exchange reactions of H with hydrogen and oxygen ions in the geocorona influence both the ionosphere and plasmasphere and enable energetic neutral atom imaging of the ring current.

Measurements of H are scarce. There is a long-standing lack of direct, mass spectrometer measurements of H abundance. Knowledge about the H distribution is based primarily on ground-, rocket-, and satellite-based remote sensing techniques [e.g., Sharp and Kita, 1987; Thomas, 1990; Bishop, 2001; Mierkiewicz et al., 2006, 2012; Kaufmann et al., 2013; Waldrop and Paxton, 2013; Qin and Waldrop, 2016; Qin et al., 2017]. In the mesopause region, observation of H is difficult from orbiting satellites or by in situ remote sensing techniques because there are no directly observable thermal infrared or visible transitions associated with H to facilitate its measurement. Consequently, H specification in the NRL Mass-Spectrometer-Incoherent-Scatter (NRLMSISE-00, hereafter simply “MSIS”) empirical model [Picone et al., 2002, and references therein] is still largely based on the Atmosphere Explorer (AE) satellite measurements of H^+ and O^+ densities, and neutral atomic oxygen density near and above 250 km. The H distribution is inferred under the assumption of charge exchange equilibrium at these heights. Extension of the hydrogen vertical profile to altitudes below 250 km is based on a diffusive equilibrium assumption with ad hoc adjustments for flow and chemistry effects, which can lead to errors in H of a factor of 2 or larger [e.g., Bishop, 2001]. For example, the MSIS H profile differs in shape and is lower in magnitude over most altitudes than the H profiles retrieved from ground-based nighttime hydrogen emission observations [Bishop et al., 2001; Bishop et al., 2004]; forward modeling using the MSIS model extended to exospheric altitudes using the Bishop analytic model indicate discrepancies in the underlying H distribution for both solar minimum and maximum conditions [Nossal et al., 2012]; and MSIS appears to overestimate upper thermospheric H density compared to the H density retrieved from the Global Ultra-Violet Imager (GUVI) onboard the TIMED satellite during daytime conditions, by 42-74% at solar maximum and 36-67% at solar minimum [Waldrop and Paxton, 2013].

As discussed above, H is produced by physical and chemical processes lower in the atmosphere that involve greenhouse gases (H_2O and CH_4); H produces H^+ through charge exchange reactions, and this H^+ is an important source of H^+ in the magnetosphere and plasmasphere; in addition, the escape of H above the exobase is the process by which the Earth's water is eventually lost. Therefore, understanding H and its variability will better advance our understanding of the Earth's climate, the magnetosphere and plasmasphere, and the Earth's water budget. Thus, it is important to advance our current understanding of hydrogen variability and improve the empirical specification of hydrogen variability in MSIS.

Here, we investigate this atomic hydrogen variability from the mesopause region to the upper thermosphere, on solar cycle, seasonal, and diurnal time scales, using data and model simulations. We use atomic hydrogen data derived from the measurements made by the Sounding of the Atmosphere using Broadband Emission Radiometry (SABER) instrument on the Thermosphere Ionosphere Mesosphere Energetics Dynamics (TIMED) satellite [Mlynczak et al., 2014]. The H data derived from ongoing SABER measurements, starting in 2002, span more than a solar cycle, providing an unprecedented long-term hydrogen dataset in the mesopause region. Atomic hydrogen and the other HO_x species are included in the National Center for Atmospheric Research (NCAR) Whole Atmosphere Community Climate Model - eXtended (WACCM-X) [Liu et al., 2010; Liu et al., 2017; J. Liu et al., 2017], providing a global model simulation of HO_x chemistry and transport. We also compare these observational and modeling results with atomic hydrogen specified by MSIS. Section 2 gives brief descriptions of the data and the model; section 3 presents hydrogen variability; section 4 provides some further discussion of the hydrogen variability; and section 5 concludes the study.

2. Data and Model

2.1 TIMED/SABER Atomic Hydrogen

Atomic hydrogen abundance is derived from the SABER measurement of the OH volume emission rate near 2.0 μm, for both day and night, in the mesopause region (~ 80 – 100 km). SABER observes vertical profiles of spectrally integrated limb radiance ($W/m^2/sr$). The SABER instrument is extremely sensitive and measures the limb radiance profile at high precision in the mesopause region, with peak signal-to-noise ratios of 100 to 1000 at night [Mlynczak et al., 2013], and peak signal-to-noise ratios of 20 to 250 during daytime [Mast et al., 2013]. Approximately 1500 limb radiance profiles are recorded in a 24 h period. The SABER OH 2.0 μm volume emission rate V is directly related to the reaction of hydrogen and ozone. Hydrogen concentration is derived based on the excited OH chemical system model [Mlynczak et al., 2014] that is also used to retrieve nighttime atomic oxygen [e.g., Smith et al., 2010; Mlynczak et al., 2013]. At night, atomic H number density is derived assuming that photochemical balance exists between the production of O_3 by atomic and molecular oxygen three-body recombination and the loss of O_3 by reaction with H; the retrieval uses the density of atomic oxygen, the O_3 (from SABER measurements of 9.6 μm emission), and the temperature (retrieved independently from SABER 15 μm measurements). During the day, O_3 production by the atomic and molecular oxygen three-body recombination is balanced by photolysis of O_3 in the Hartley band. From this balance, daytime O is derived using SABER daytime ozone, temperature, and pressure [e.g., Smith et al., 2010]. Daytime H is then directly derived from the OH volume emission rate using the SABER daytime O, O_3, and temperature, and pressure. The latter two parameters are used to derive total number density, N_2, and O_2 densities. For both day and night, a profile of H is derived for each measured limb radiance profile. For the SABER H retrieval, day is defined as the case when solar zenith angles are less than 85°, night is defined as having solar zenith angles greater than 95°. Please refer to Mlynczak et al., 2014 for a detailed description of SABER day and night hydrogen retrieval. These individual profiles of H are available from the SABER data archive as routine products. In this paper, we will focus on the region between ~ 85 km and 95 km. Below ~ 85 km, the SABER day ozone possessing has a daytime high bias near 80–85 km [Smith et al., 2013], which results in a smaller than actual H concentration; above ~ 95 km, there are also uncertainties in the daytime ozone abundance [Mlynczak et al., 2014].

2.2 WACCM-X

The Whole Atmosphere Community Climate Model (WACCM) is one of the atmospheric models that make up the NCAR Community Earth System Model (CESM). CESM is a coupled model consisting of atmosphere, ocean, land surface, sea and land ice, and carbon cycle components for simulating past, present, and future climates. These components are linked through a coupler that exchanges fluxes and state information among them. More detailed information on CESM can be found at http://www.cesm.ucar.edu/. WACCM is a whole atmosphere climate-chemistry general circulation model developed at NCAR. It is based upon the infrastructure of the Community Atmosphere Model (CAM), which is the atmospheric component of CESM, with vertical domain extending to 5.9 $x10^{-6}$ hPa (~ 140 km geometric height). The chemistry module of WACCM is interactive with dynamical transport and exothermic heating [Kinnison et al., 2007]. WACCM chemistry is based on the MOZART model [Kinnison et al., 2007], which includes all of the reactions that are known to be important for the middle and upper atmosphere, including all the odd hydrogen chemistry in this region. Tropospheric source gases for the members of the hydrogen, chlorine, bromine, nitrogen, and hydrocarbon families vary with season and year based on changing emissions and other factors [Emmons et al., 2010]. The model simulates 74 chemical species, representing the gas-phase, heterogeneous, and photolytic reactions that link them. Photochemistry associated with ion species (O^+, NO^+, O_2^+, N_2^+, N^+, and metastable O^+ states) is part of the chemistry package. Details of WACCM can be found in Garcia et al. [2007], Smith et al. [2011], and Marsh et al. [2013]. WACCM extended into the ionosphere/thermosphere (called WACCM-X) has a top boundary at the upper thermosphere ($4.5x10^{-10}$ hPa, or ~700 km). Details of an earlier version of WACCM-X can be found in Liu et al. [2010]. Recently we have developed a more self-consistent ionosphere module for WACCM-X that includes the computation of electron and ion temperatures, an interactive electric wind dynamo, and O^+ transport in the ionospheric F-region. WACCM-X now produces ionospheric structures that are in good agreement with observations [Liu et al., 2017; J. Liu et al., 2017]. The dynamical core of the model has been recently improved to represent the species dependency of specific heats and mean atmosphere mass in the thermosphere. WACCM-X can be configured either for free-running climate simulations (lower atmosphere unconstrained), or with the lower-middle atmosphere constrained by meteorology. In this study, we employ WACCM-X in the free-running climate simulation configuration.

2.3. The MSIS Empirical Atmosphere Model

We use the latest version of the MSIS series of models, NRLMSISE-00 [Picone et al., 2002]. NRLMSISE-00 extends from the ground to the exobase. The model consists of analytic formulations for the vertical structure of the atmosphere as a function of geophysical location, time, solar activity, and geomagnetic activity, based on our physical understanding of the atmosphere [Hedin, 1987]. The datasets that are used to fit those analytical formulations include total mass density from satellite accelerometers and orbit determination, temperature from incoherent scatter radars, and O_2 number density from solar ultraviolet occultations measured by the Solar Maximum Mission. The model provides altitude profiles of temperature T(z), number densities of species (He, O, N_2, O_2, Ar, H, N) in equilibrium at the temperature T(z), total mass density, and the number density of a high altitude ‘‘anomalous oxygen’’ component of total mass density that is not in thermal equilibrium at T(z). H specification in the model is based on AE measurements of H^+ and O^+ densities, and neutral atomic oxygen density near and above 250 km under the assumption of charge exchange equilibrium at thermospheric heights [Brinton et al., 1975; Waldrop et al., 2006]. Extension of the hydrogen vertical profile to altitudes below is based on diffusive equilibrium with adjustments for flow and chemistry effects. Please refer to Picone et al. [2002] and references therein for the detailed description of the model.

3. Results

WACCM-X uses a parameterization scheme to specify EUV (Extreme Ultra-Violet) and X-ray irradiance from 0.05 nm – 121 nm, which takes as input the $F_{10.7}$ (10.7 cm solar radio flux) and $F_{10.7a}$ (81-day average $F_{10.7}$) [Solomon and Qian, 2005]. The specification of solar spectral irradiance from Lyman-α (121.6 nm) to the near infrared uses the empirical model of Lean et al. [2005]. We ran WACCM-X for solar minimum ($F_{10.7}$=70) and solar maximum ($F_{10.7}$=200) conditions. Geomagnetic activity was set to be quiet for solar minimum conditions (K_p=1) and moderate for solar maximum conditions (K_p=3). These runs were free-running climate simulations with the lower atmosphere unconstrained. In each case, the model was run for two years, the first year to allow the model to fully equilibrate, and the second year to obtain results for analysis.

The model-simulated atomic hydrogen abundance was compared to the atomic hydrogen abundance retrieved from SABER observations in the mesopause region (~ 85 – 95 km), as well as to the atomic hydrogen calculated by MSIS in this region and in the thermosphere. The comparisons were made for both atomic hydrogen volume mixing ratio (vmr) and number density. Using either volume mixing ratio or number density does not qualitatively change the results.

Figure 1 shows the global and annual average hydrogen from SABER in vmr (figure 1a) and in number density (figure 1c), for 2003 and 2008, and the corresponding H abundance simulated by WACCM-X under solar minimum and maximum conditions (figures 1b, 1d). It is evident that above ~ 85 km, which is the mesopause region that we focus on in this paper, there is more H at solar minimum than at solar maximum, in both vmr and number density. The solar cycle variability of SABER H density in this region is on the order of ~ 10%, on a global average basis. Similarly, the H vmr and number density simulated by WACCM-X show the same relation with solar activity in the 85-95 km altitude range, although with a smaller magnitude, at ~ 5% on a global average basis for H density. This is interesting since the primary source of hydrogen in this region is the photolysis of H_2O at Lyman-α, and Lyman-α irradiance increases proportionally to solar activity. The observed and modeled solar cycle changes are small, especially compared to the uncertainties involved in estimating H from SABER data. The absolute uncertainties in SABER H density estimation stem from uncertainties in the O and O_3 determination, and HO_x chemistry rate coefficients. The uncertainties for the day and night retrieval of hydrogen are comparable, at ~ 35% [Mlynczak et al., 2014]. However, it is important to note that when looking at temporal variability of atomic hydrogen, the uncertainties of H retrieval are always in the same direction. If the retrieved H is too large at solar maximum, then it is also too large at solar minimum, and these uncertainties cancel to first order [Mlynczak et al., 2014]. Since the solar cycle variation is subtle, and requires a stable measurement over ~11 years, the strongest conclusion we can draw from the data-model comparison is that they are qualitatively consistent.

Figure 2 shows the global annual average H number density profiles from the mesopause to the upper thermosphere, specified by MSIS and simulated by WACCM-X, under solar minimum ($F_{10.7}$=70) and solar maximum conditions ($F_{10.7}$=200). The H density specified by MSIS (figure 2a, 2c) has an inverse relation with solar activity from the mesopause region to the upper thermosphere, whereas the solar activity dependence of H density simulated by WACCM-X (figures 2b, 2c, 2d) changes sign twice: in the mesopause region ~ 85 – 95 km, there is more hydrogen at solar minimum than at solar maximum (consistent with SABER), on the order of ~ 5%; in the lower thermosphere ~ 95 – 130 km, there is more hydrogen at solar maximum than at solar minimum (figures 2c and 2d), on the order of ~ 10%, and then above ~ 130 km, there is significantly more hydrogen at solar minimum than solar maximum (consistent with MSIS), and the solar cycle amplitude is a factor of ~ 10 from both WACCM-X and MSIS. The inverse relation between hydrogen density and solar activity in the upper thermosphere is supported by the H density derived from the Lyman alpha radiance measurements by GUVI [Waldrop and Paxton, 2013; Qin and Waldrop, 2016; Qin et al., 2017]. We also conducted simulations using the NCAR global mean (GLBM) version of the TIME-GCM (Thermosphere Ionosphere Mesosphere Electrodynamics General Circulation Model) [Roble et al., 1987; Roble and Ridley, 1994]. The results are shown in figure 2b as the dashed line. It is evident that the solar cycle variability of H density simulated by GLBM is qualitatively consistent with the results from WACCM-X: in the lower thermosphere ~ 95 – 130 km, H density is larger at solar maximum than at solar minimum (figures 2b and 2d); above ~ 130 km, H density at solar minimum is larger than the H density at solar maximum. By 300 km, it is 10 times larger (figure 2b). Although there is no observational evidence yet that the solar cycle variability of H density in the 95–130 km altitude range is different from the solar cycle variability in the upper thermosphere, the qualitative agreement between GLBM and WACCM-X is significant and is worth exploring further in the future.

The TIMED satellite executes a 180-degree rotation about its yaw axis every 60 days to keep the Sun from illuminating the thermal radiators of the instruments onboard the satellite; observational local times shift through a yaw period due to the earth's orbital precession but almost all local times (day and night) are sampled within each yaw period. We calculate yaw-cycle averaged atomic hydrogen vmr in order to examine the seasonal variability of atomic hydrogen. Figure 3 shows yaw-cycle averaged H vmr derived from SABER measurements, representing the December (the yaw cycle 2002325 – 2003015) and June solstices (the yaw cycle

2003142 – 2003198) under solar maximum conditions, and the December (the yaw cycle 2007323 – 2008013) and June solstices (the yaw cycle 2008140 – 2008195) under solar minimum conditions. It is evident that, in both the December and June solstices, and under both solar minimum and maximum conditions, hydrogen vmr in the mesopause region (~ 85 – 95 km) is larger in the summer hemisphere than in the winter hemisphere.

Figure 4 shows 2-month averaged zonal-mean hydrogen vmr simulated by WACCM-X, representing the December and June solstices under solar maximum ($F_{10.7}$=200) and minimum ($F_{10.7}$=70) conditions. Above ~ 85 km, the seasonal distribution of the simulated hydrogen is consistent with the observed seasonal variability: H vmr is larger in the summer hemisphere than it is in the winter hemisphere. The magnitudes of the observed and simulated H vmr are also in good agreement.

MSIS gives H vmr in the upper thermosphere (~ 300 km) that is larger in winter than in summer (figure 5a). This is consistent with our knowledge of the seasonal distribution of lighter species; for example, the often-observed winter helium bulge phenomenon [e.g., Reber et al., 1968; Keating and Prior, 1968; Kockarts, 1972]. So, the question is: at which altitude does H change its seasonal variation, from being larger in summer than in winter in the mesopause region, to being larger in winter than in summer in the upper thermosphere?

Figure 5 shows the zonal-mean hydrogen vertical profiles at 50^{o}S and 50^{o}N, representing the December and June solstices, under solar maximum ($F_{10.7}$ = 200) and geomagnetically quiet conditions, that are specified by MSIS and simulated by WACCM-X. The corresponding SABER zonal-mean hydrogen vmr vertical profiles are also shown. For both the December and June solstice conditions, the seasonal distribution of MSIS H indicates concentrations that are larger in winter than in summer, from the mesopause to the upper thermosphere. Therefore, in the mesopause region, the summer-winter distribution of H in MSIS contradicts the results from SABER observations (figures 5a, 5c). On the other hand, in the mesopause region, the WACCM-X-simulated H vmr shows a seasonal distribution that is consistent with the results from SABER observations (figures 5b, 5d): H vmr is larger in summer than in winter, although the WACCM-X-simulated H vmr is smaller than the H vmr estimated by SABER in the winter hemisphere. The WACCM-X-simulated seasonal distribution of H vmr switches sign from a summer maximum to a winter maximum at ~ 130 km. Above ~ 130 km, the seasonal dependence of H vmr simulated by WACCM-X and calculated by MSIS are in good agreement. H vmr is larger in the winter hemisphere than it is in the summer hemisphere. In the upper thermosphere, the seasonal amplitude of both H vmr and H number density (not shown) is on the order of a factor of ~ 2.

Figure 6 shows the diurnal variation of hydrogen density at 45^{o}S and 0^o longitude, on December 1st, under solar minimum and geomagnetically quiet conditions, simulated by WACCM-X (figure 6a), and calculated by MSIS (figure 6b). The diurnal variations in WACCM-X and MSIS are in general agreement: H density is larger at night than it is during daytime; H density maximizes at ~ 3am, and minimizes in the afternoon, ~ 3pm for MSIS but later for WACCM-X, ~ 5pm. In the upper thermosphere, the diurnal amplitude is on the order of a factor of ~ 2.

4. Discussion

In the mesosphere, hydrogen is primarily produced as a result of the photolysis of water vapor (H_2O) by Lyman-α. Water enters the middle atmosphere through transport from the troposphere and oxidization of CH_4 in the stratosphere [Brasseur and Solomon, 2005]. The maximum mixing ratio of H_2O in the middle atmosphere occurs in the lower mesosphere. In the mesopause region, there is more H_2O in summer than in winter due to the upwelling of the mesospheric meridional circulation [e.g., Rong et al., 2010]; this combined with the longer periods of daylight leads to more production of atomic hydrogen. Another example of the close relation between atomic hydrogen and H_2O concentration is the depletion of H in the summer polar region. Siskind et al. [2008] analyzed H retrieved from SABER observations and found that there is a surprising decrease of H in the polar region in the summer hemisphere, and model simulations showed that it is caused by the sequestering of H_2O by the formation of polar mesospheric clouds.

In the thermosphere, the charge exchange reactions that affect atomic hydrogen have a relatively small contribution to the total hydrogen budget compared to dynamics. Vertical winds are critically important for thermospheric major species, since their strongest gradients are in the vertical. However, H has a scale height of 200 km – 800 km in the isothermal upper thermosphere, and thus is less directly influenced by vertical winds than the major species since the H mixing ratio is fairly uniform with altitude. Therefore, it might be reasonable to assume that H would undergo relatively few changes in the upper thermosphere. However, we have seen from figures 1-6 that in the upper thermosphere, atomic hydrogen density varies on time scales of solar cycle, seasonal, and diurnal by factors of ~ 10, ~ 2, and ~ 2, respectively. Therefore, the question is what processes drive such large variability? What determines the transition of H abundance from the seasonal and solar cycle structure in the mesopause region that is more characteristic of the middle atmosphere to the opposite seasonal and solar cycle variability in the thermosphere?

Atomic hydrogen concentration is determined by the hydrogen continuity equation, with terms including horizontal and vertical advections, photochemical production and loss, eddy diffusion, and molecular diffusion. Since H is the lightest species, its molecular weight is significantly different from the mean molecular mass. Therefore, the molecular diffusion process is worth mentioning here. According to Banks and Kockarts [1973], the diffusing of a minor species, such as H, through a background atmosphere composed of the dominant species (N_2, O_2, O) can be expressed as:

$$X_D = \frac{1}{\rho_0}\frac{\partial}{\partial z}\left(\rho_0 D_\mu \frac{\partial \mu}{\partial z}\right) - \frac{1}{\rho_0}\frac{\partial}{\partial z}(\rho_0 \mu w_D) \quad (1)$$

and

$$w_D = \frac{D_\mu}{h}\left(1 - \frac{h}{h_\mu}\right) \quad (2)$$

Where μ is the hydrogen mixing ratio. z is the vertical coordinate, ρ_0 is the atmosphere mass density. D_μ is the molecular diffusion coefficient, which is dependent on the mean molecular mass of the major species, the molecular mass of the minor species, total number density, and temperature [Banks and Kockarts, 1973]. It is important to note that, in an atmospheric numerical model, the continuity, momentum, and energy equations are often expressed using the mixing ratio of a species instead of number density since the simple compression of air modifies the number density but not the mixing ratio. Consequently, using the mixing ratio simplifies the equations so that the equations can more easily be solved numerically. $h = \frac{kT}{Mg}$ is the scale height of the background atmosphere, and $h_\mu = \frac{kT}{M_\mu g}$ is the scale height of atomic hydrogen. k is the Boltzmann's constant, g is the acceleration of gravity, and M and M_μ are the mean molecular mass of the background atmosphere and the molecular mass of hydrogen, respectively. It is evident from equations (1) and (2) that molecular diffusion includes a diffusive term that depends on the mixing ratio gradient, and a second term that measures the diffusive separation between hydrogen and the background gas. w_D is essentially the diffusive separation velocity. It is determined by the relative mass of a species and the background atmosphere, so that molecules that are heavier than the background atmosphere drift downward while those that are lighter drift upward. Since H is the lightest species, its molecular weight is significantly different from the mean molecular mass; its diffusive separation velocity w_D is the largest among all species.

It is evident that when a minor species diffuses through a background atmosphere, both the eddy diffusive mixing term and the diffusive separation term (equation (1)) depend on the densities of the major species. Atomic hydrogen density itself also depends on the densities of the major species since it is the multiplication of its volume mixing ratio and the total number density of the major species. Therefore, various complex dynamical processes, including both the minor species diffusion process, which is specific to the minor species, as well as major species dynamics, should play role in determining atomic hydrogen abundance and its variability. We hypothesize that the diffusive separation velocity term and how it reacts to major species dynamics might be the mechanism that drives the large and unique variability of hydrogen in the thermosphere. Our future work is to conduct diagnostic analysis to understand the physical processes that drives these large, unique variabilities of hydrogen on various time scales.

5. Summary

It is important to advance our understanding of hydrogen variability in the upper atmosphere in order to advance our understanding of the Earth's climate, the magnetosphere and plasmasphere, and the Earth's water budget. Recent comparisons of H specified by MSIS and the

H density retrieved from GUVI indicate that during daytime conditions, MSIS appears to overestimate H density in the upper thermosphere by ~ 50% for both solar minimum and solar maximum conditions [Waldrop and Paxton, 2013].

The availability of the atomic hydrogen dataset retrieved from SABER from 2002 to 2017, and the whole atmosphere model WACCM-X [Liu et al., 2017] provide us the opportunity to investigate hydrogen variability from the mesopause region to the upper thermosphere, to assess the hydrogen specification in MSIS, and provide knowledge and guidance to improve the specification of the hydrogen vertical profile and its variability in MSIS. We conducted WACCM-X simulations to examine atomic hydrogen and its variability from the mesopause to the upper thermosphere, on solar cycle, seasonal, and diurnal time scales. We compared model simulation results to the H abundance retrieved from SABER observations in the mesopause region, and to the H specified by MSIS from the mesopause region to the upper thermosphere. We found that:

(1) In the mesopause region (~ 85 – 95 km), SABER observations and WACCM-X simulations show that there is slightly more hydrogen at solar minimum than at solar maximum. On a global average basis, the solar cycle amplitudes of H density are on the order of ~ 10% and ~ 5%, from SABER observations and WACCM-X simulations, respectively.

(2) WACCM-X simulations show that H switches the sign of its solar cycle dependence twice: in the altitude range ~ 95 – 130 km, there is more hydrogen at solar maximum than at solar minimum, inverse to the regions above and below. This result is supported by simulation results from the global mean version of the NCAR/TIME-GCM. On a global average basis, the solar cycle amplitude of H density in this region simulated by WACCM-X is on the order of ~ 10%. This switch in the sign of solar cycle dependence is not seen in MSIS, where there is more

hydrogen at solar minimum than at solar maximum, from the mesopause through the upper thermosphere. Although there is no observational evidence yet that the solar cycle variability of H in the lower thermosphere (95–130 km) is different from the solar cycle variability in the upper thermosphere, the qualitative agreement between GLBM and WACCM-X is significant and is worth further exploration.

(3) In the upper thermosphere, both MSIS and WACCM-X indicate that there is about an order of magnitude higher hydrogen density at solar minimum than at solar maximum. The solar cycle amplitude of H density simulated by WACCM-X is in good agreement with that calculated by MSIS. It is on the order of ~ 10 from both MSIS and WACCM-X.

(4) In the mesopause region (~ 85 – 95 km), the seasonal variation of atomic hydrogen simulated by WACCM-X is in good agreement with what is derived from SABER observations. Atomic hydrogen vmr is larger in the summer hemisphere than it is in the winter hemisphere. However, atomic hydrogen vmr specified by MSIS is larger in the winter hemisphere than in the summer hemisphere, which contradicts the simulations by WACCM-X and the observations by SABER. MSIS developers are aware of the issues regarding H (and other species), due the limitations of previous data sets. These will be addressed in future versions of the MSIS model [Douglas P. Drob, personal communication, 2017].

(5) The seasonal dependence of H mixing ratio simulated by WACCM-X changes sign at ~ 130 km. Above ~ 130 km, the seasonal dependence of H vmr simulated by WACCM-X and calculated by MSIS are in good agreement. H vmr is larger in the winter hemisphere than it is in the summer hemisphere. The seasonal amplitude of both H vmr and H density is on the order of a factor of ~ 2.

(6) The diurnal variation of atomic hydrogen density simulated by WACCM-X is consistent with what is calculated by MSIS. Hydrogen density is larger during nighttime than it is during daytime; hydrogen density maximizes at ~ 3 am in both WACCM-X and MSIS, and it minimizes at ~ 3 pm for MSIS but later for WACCM-X, ~ 5pm. In the upper thermosphere, the diurnal amplitude of H density is on the order of ~ 2.

In addition to the large variabilities on various time scales, the behavior of atomic hydrogen is unique compared to the major species. For example, the current WACCM-X simulations indicate that no major species in the thermosphere switches solar cycle dependence as hydrogen does. On the other hand, both the hydrogen diffusion processes and atomic hydrogen density itself depend on the densities of the major species. Therefore, various complex dynamical processes, including both the minor species diffusion process, as well as major species dynamics, likely play a role in determining atomic hydrogen abundance and its variability. Future work will investigate how dynamical forcing acts differently for the major species and atomic hydrogen to drive this behavior, and thus to deepen our understanding of the thermosphere dynamics.

Acknowledgements. This research was supported by NASA grants NNH15ZDA001N-HSR, NNX13AE20G, NNX14AE06G, NNX15AB83G, NNX15AJ24G, NNX14AD83G, NNX15AJ24G, and NNX14AC13G, to the National Center for Atmospheric Research. NCAR is sponsored by the National Science Foundation. We would like to thank the SABER team for the atomic hydrogen dataset. SABER is supported by NASA grant NNX12AG45G. SABER atomic hydrogen data are available from the SABER data archive as routine products at saber.gats-inc.com. WACCM-X is an open-source community model, and all model simulation results used in this paper are archived on the NCAR High Performance Storage System, and are available upon request.

References

Anderson, D. E. Jr., L. J. Paxton, R. P. McCoy, R. R. Meier, and S. Chakrabarti (1987), Atomic hydrogen and solar Lyman alpha flux deduced from STP 78-1 UV observations, J. Geophys. Res., 92, 8759–8766.

Banks, P. M., and G. Kockarts (1973), Aeronomy: Part B, Academic, San Diego, Calif.

Bishop, J. (2001), Thermospheric atomic hydrogen densities and fluxes from dayside Lyman alpha measurements, J. Atmos. Sol. Terr. Phys., 63, 331–340.

Bishop, J., J. Harlander, S. Nossal, and F. L. Roesler (2001), Analysis of Balmer alpha intensity measurements near solar minimum, J. Atmos. Sol. Terr. Phys., 63, 341–353.

Bishop, J., E. J. Mierkiewicz, F. L. Roesler, J. F. Gómez, and C. Morales (2004), Data-model comparison search analysis of coincident PBO Balmer alpha EURD Lyman beta geocoronal measurements from March 2000, J. Geophys. Res., 109, A05307, doi:10.1029/2003JA010165.

Brasseur, G., and S. Solomon (2005), Aeronomy of the Middle Atmosphere, 3rd ed., Springer, Dordrecht, Netherlands.

Brinton, H. C., H. G. Mayr, and W. E. Potter (1975), Winter bulge and diurnal variations in hydrogen inferred from AE-C composition measurements, Geophys. Res. Lett., 2, 389–392.

Chamberlain, J. W., and D. M. Hunten (1987), Theory of Planetary Atmospheres: An Introduction to their Physics and Chemistry, 2nd ed., Academic, San Diego, Calif.

Emmons, L. K., et al. (2010), Description and evaluation of the Model for Ozone and Related chemical Tracers, version 4 (MOZART-4), Geosci. Model Dev., 3, 43–67, doi:10.5194/gmd-3-43-2010.

Garcia, R. R., D. R. Marsh, D. E. Kinnison, B. A. Boville, and F. Sassi (2007), Simulation of secular trends in the middle atmosphere, 1950– 2003, J. Geophys. Res., 112, D09301, doi:10.1029/2006JD007485.

Hedin, A. E. (1987), MSIS-86 thermospheric model, J. Geophys. Res., 92, 4649–4662.

Kaufmann, M., M. Ern, C. Lehmann, and M. Riese (2013), The response of atomic hydrogen to solar radiation changes, in Climate and Weather of the Sun-Earth System, pp. 171–188, Springer, Dordrecht, doi:10.1007/978-94-007-4348-9.

Keating, G., and E. Prior (1968), The winter helium bulge, Space Res., 8, 982.

Kinnison, D. E., et al. (2007), Sensitivity of chemical tracers to meteorological parameters in the MOZART-3 chemical transport model, J. Geophys. Res., 112, D20302, doi:10.1029/2006JD007879.

Kockarts, G. (1972), Distribution of hydrogen and helium in the upper atmosphere, J. Atmos. Terr. Phys., 34, 1729-1743.

Lean, J., G. Rottman, J. Harder, and G. Kopp (2005), Sorce contributions to new understanding of global change and solar variability, Solar Physics, 230, 27–53, doi: 10.1007/s11207-005-1527-2.

Liu, H. - L., et al. (2010), Thermosphere extension of the Whole Atmosphere Community Climate Model, J. Geophys. Res., 115, A12302, doi:10.1029/2010JA015586.

Liu, H. -L., C. G. Bardeen, B. T. Foster, P. Lauritzen, J. Liu, G. Lu, D. R. Marsh, A. Maute, J. M. McInerney, N. M. Pedatella, L. Qian, A. D. Richmond, R. G. Roble, S. C. Solomon, F. M. Vitt, W. Wang (2018), Development and Validation of the Whole Atmosphere Community Climate Model with Thermosphere and Ionosphere Extension (WACCM-X), Journal of Advances in Modeling Earth Systems, doi:10.1002/2017MS001232, in press.

Liu, J., H.-L. Liu, W. Wang, A. G. Burns, Q. Wu, Q. Gan, S. C. Solomon, D. R. Marsh, L. Qian, G. Lu, N. M. Pedatella, J. M. McInerney, J. M. R. III, and W. S. Schreiner (2018), First results from ionospheric extension of waccm-x during the deep solar mini- mum year 2008, J. Geophys. Res., doi: 10.1002/2017JA025010, submitted.

Marsh, D. R., M. E. Mills, D. E. Kinnison, J.-F. Lamarque, N. Calvo, and L. M. Polvani (2013), Climate change from 1850 to 2005 simulated in CESM1 (WACCM), J. Clim., 26, 7372–7391, doi:10.1175/JCLI-D-12-0558.1.

Mast, J., M. G. Mlynczak, L. A. Hunt, B. T. Marshall, C. J. Mertens, J. M. Russell III, R. E. Thompson, and L. L. Gordley (2013), Absolute concentrations of highly vibrationally excited OH (õ = 9 + 8) in the mesopause region derived from the TIMED/SABER instrument, Geophys. Res. Lett., 40, 646–650, doi:10.1002/grl.50167.

Mierkiewicz, E. J., F. L. Roesler, S. M. Nossal, J. Bishop, R. J. Reynolds, and L. M. Haffner (2006), Geocoronal hydrogen studies using Fabry-Perot Interferometers. Part 1: Instrumentation, observations, and analysis, JASTP, 68, 1520–1552, doi:10.1016/j.jastp. 2005.08.024.

Mierkiewicz, E. J., F. L. Roesler, and S. M. Nossal (2012), Observed seasonal variations in exospheric effective temperatures, J. Geophys. Res., 117, A06313, doi:10.1029/2011JA017123.

Mlynczak, M. G., et al. (2013), Atomic oxygen in the mesosphere and lower thermosphere derived from SABER: Algorithm theoretical basis and measurement uncertainty, J. Geophys. Res. Atmos., 118, 5724–5735, doi:10.1002/jgrd.50401.

Mlynczak,M. G., L. A. Hunt, B. T. Marshall, C. J. Mertens, D. R. Marsh, A. K. Smith, J. M. Russell, D. E. Siskind, and L. L. Gordley (2014), Atomic hydrogen in the mesopause region derived from SABER: Algorithmtheoretical basis, measurement uncertainty, and results, J. Geophys. Res. Atmos., 119, 3516–3526, doi:10.1002/ 2013JD021263.

Nossal, S. M., E. J. Mierkiewicz, and F. L. Roesler (2012), Observed and modeled solar cycle variation in geocoronal hydrogen using NRLMSISE-00 thermosphere conditions and the Bishop analytic exosphere model, J. Geophys. Res., 117, A03311, doi:10.1029/2011JA017074.

Picone, J. M., A. E. Hedin, D. P. Drob, and A. C. Aikin (2002), NRLMSISE-00 empirical model of the atmosphere: Statistical comparisons and scientific issues, J. Geophys. Res., 107(A12), 1468, doi:10.1029/2002JA009430.

Qin and Waldrop (2016), Non-thermal hydrogen atoms in the terrestrial upper thermosphere, Nat. Commun., 7, 13655.

Qin, J., L. Waldrop, and J. J. Makela (2017), Redistribution of H atoms in the upper atmosphere during geomagnetic storms, J. Geophys. Res. Space Physics, 122, 10,686–10,693, doi:10.1002/2017JA024489.

Smith, A. K., D. R. Marsh, M. G. Mlynczak, and J. C. Mast (2010), Temporal variations of atomic oxygen in the upper mesosphere from SABER, J. Geophys. Res., 115, D18309, doi:10.1029/2009JD013434.

Smith, A. K., R. R. Garcia, D. R. Marsh, and J. H. Richter (2011), WACCM simulations of the mean circulation and trace species transport in the winter mesosphere, J. Geophys. Res., 116, D20115, doi:10.1029/2011JD016083.

Thomas, R. J. (1990), Atomic hydrogen and atomic oxygen density in the mesosphere region: Global and seasonal variations deduced from Solar Mesosphere Explorer near-infrared emissions, J. Geophys. Res., 95, 16,457–16,476.

Reber, C., J. Cooley, and D. Harpold (1968), Upper atmosphere hydrogen and helium measurements from the Explorer 32 satellite, Space Res, 8, 993.

Roble, R. G., and E. C. Ridley, and R. E. Dickinson (1987), On the global mean structure of the thermosphere, *J. Geophys. Res., 92*, 8745-8758.

Roble, R. G., and E. C. Ridley (1994), A thermosphere-ionosphere-mesosphere-electrodynamics general circulation model (TIME-GCM): Equinox solar cycle minimum simulations (30-500 km), Geophys. Res. Lett., 21, 417-420.

Rong, P. P., J. M. Russell III, L. L. Gordley, M. E. Hervig, L. Deaver, P. F. Bernath, and K. A. Walker (2010), Validation of v1.022 mesospheric water vapor observed by the Solar Occultation for Ice Experiment instrument on the Aeronomy of Ice in the Mesosphere satellite, J. Geophys. Res., 115, D24314, doi:10.1029/2010JD014269.

Sharp, W. E., and D. Kita (1987), In situ measurement of atomic hydrogen in the upper mesosphere, J. Geophys. Res., 92, 4319–4324.

Siskind, D. E., D. R. Marsh, M. G. Mlynczak, F. J. Martin-Torres, and J. M. Russell III (2008), Decreases in atomic hydrogen over the summer pole: Evidence for dehydration from polar mesospheric clouds? Geophys. Res. Lett., 35, L13809, doi:10.1029/2008GL033742.

Solomon, S. C., and L. Qian (2005), Solar extreme-ultraviolet irradiance for general circulation models, J. Geophys. Res., 110, A10306, doi:10.1029/2005JA011160.

Waldrop, L. S., E. Kudeki, S. A. González, M. P. Sulzer, R. Garcia, M. Butala, and F. Kamalabadi (2006), Derivation of neutral oxygen density under charge exchange in the midlatitude topside ionosphere, J. Geophys. Res., 111, A11308, doi:10.1029/2005JA011496.

Waldrop, L., and L. J. Paxton (2013), Lyman alpha airglow emission: Implications for atomic hydrogen geocorona variability with solar cycle, J. Geophys. Res. Space Physics, 118, 5874–5890, doi:10.1002/jgra.50496.

Woods, T., and G. Rottman (2002), Solar ultraviolet variability over time periods of aeronomic interest, in Atmospheres in the Solar System: Comparative Aeronomy, Geophys. Monogr. Ser., vol. 130, edited by M. Mendillo, A. Nagy, and J. H. Waite Jr., pp. 221–234, AGU, Washington, D. C.

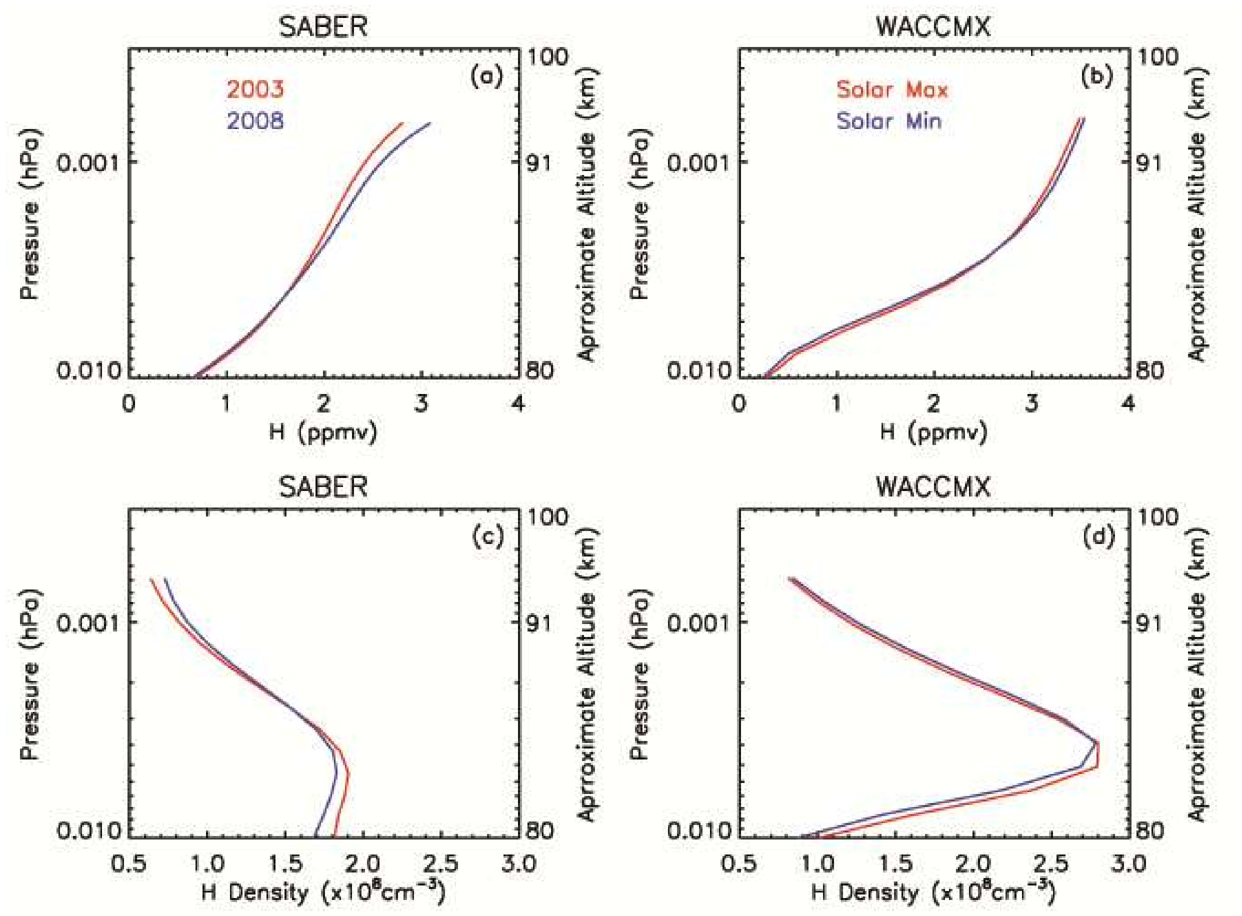

Figure 1: Solar-cycle variation of global annual average hydrogen in the mesopause region. (a) SABER H vmr for 2003 and 2008; (b) H vmr simulated by WACCM-X under solar maximum (F10.7=200) and solar minimum (F10.7=70) conditions; (c) same as (a), but for H number density; (d) same as (b), but for H number density.

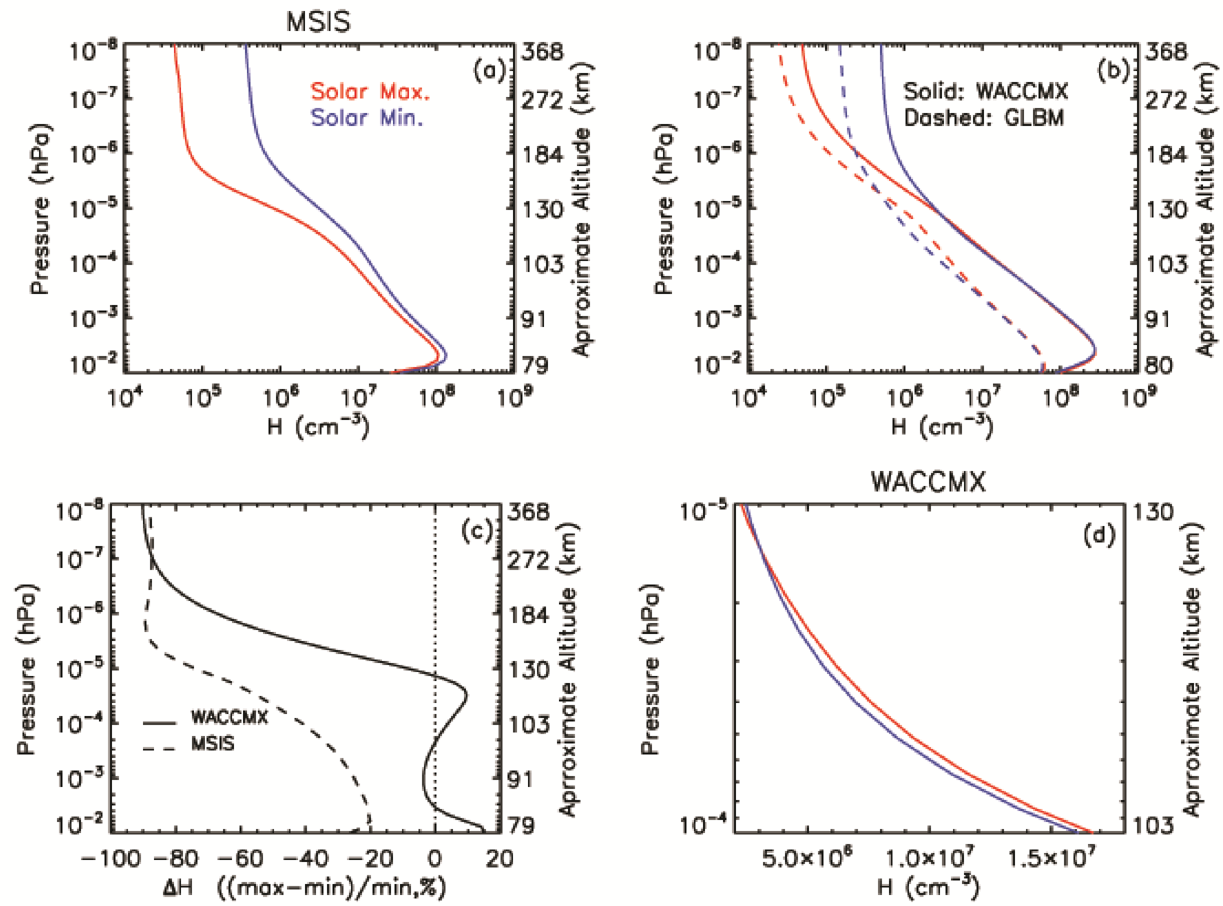

Figure 2: Solar cycle variations ($F_{10.7}$=70 versus $F_{10.7}$=200) of hydrogen density. (a) Calculated by MSIS; (b) simulated by WACCM-X and GLBM; (c) difference between solar minimum and maximum conditions (max-min)/min; (d) simulated by WACCM-X in the altitude region ~ 100 – 130 km;

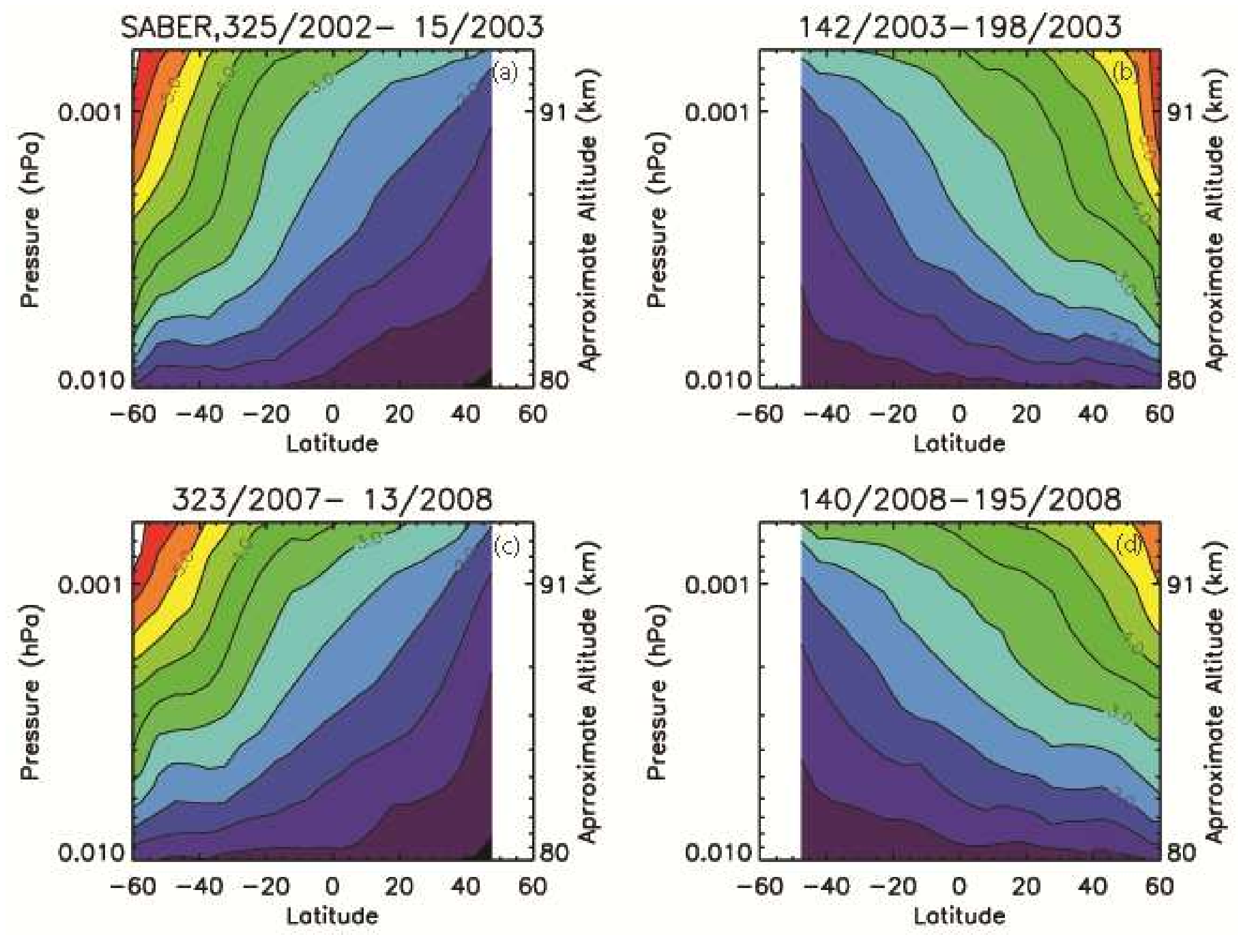

Figure 3: Yaw-cycle averaged zonal-mean hydrogen vmr (ppmv) derived from SABER measurements. (a) The yaw cycle that includes the December solstice in 2003; (b) the yaw cycle that includes the June solstice in 2003; (c) the yaw cycle that includes the December solstice in 2007; (d) the yaw cycle that includes the June solstice in 2008.

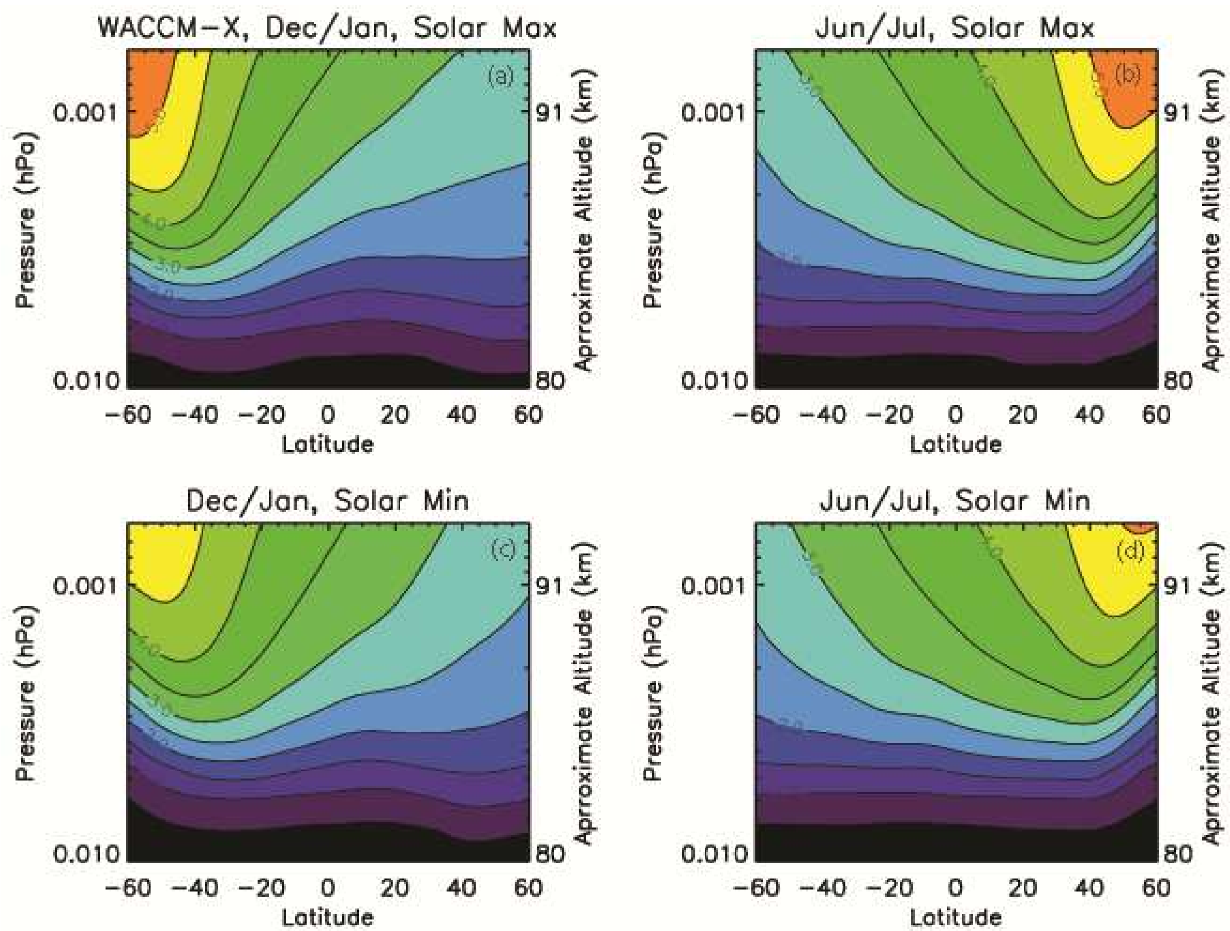

Figure 4: 2-month averaged zonal-mean hydrogen vmr (ppmv) simulated by WACCM-X under solar minimum and maximum, and geomagnetically quiet conditions. (a) December and January averages representing the December solstice at solar maximum; (b) June and July averages representing the June solstice at solar maximum; (c) December and January averages representing the December solstice at solar minimum; (b) June and July averages representing the June solstice at solar minimum.

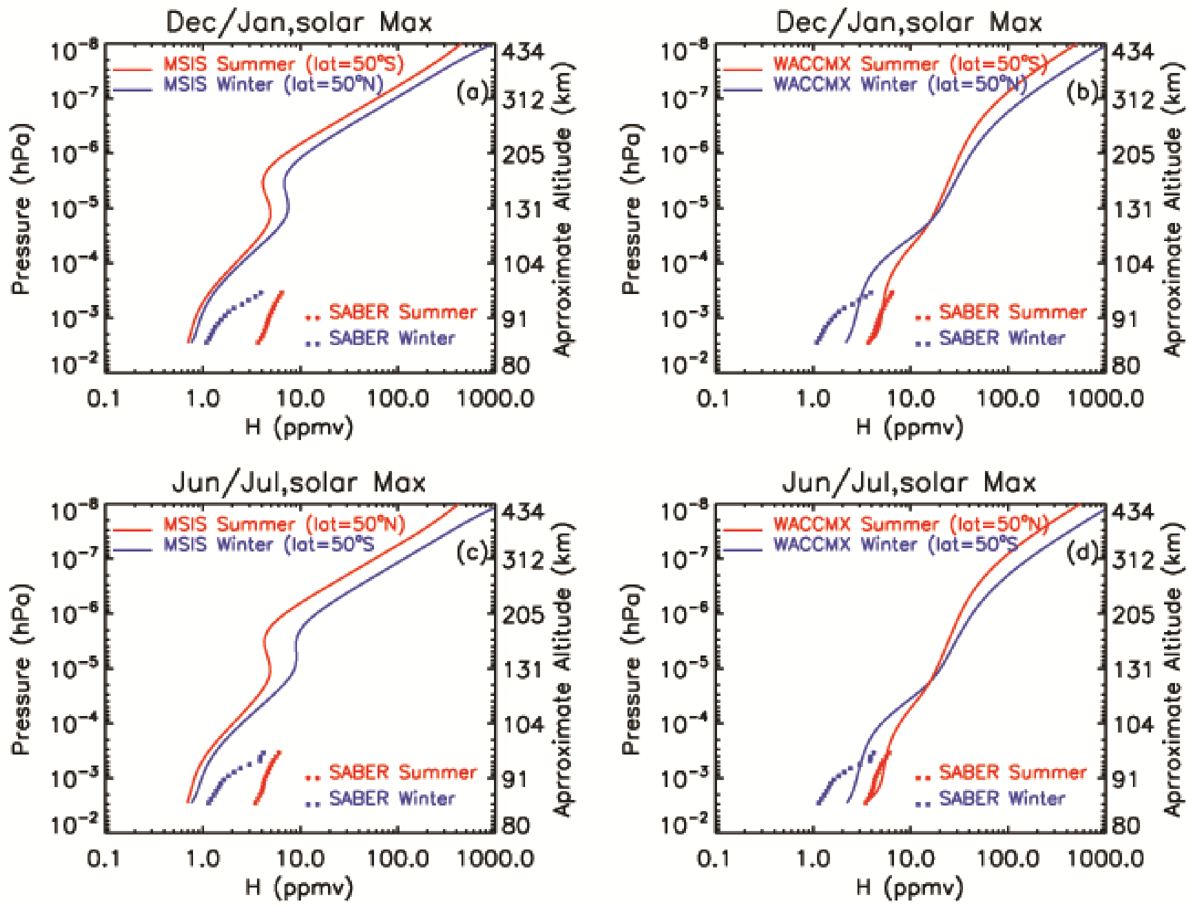

Figure 5: Zonal-mean vertical profiles of hydrogen vmr at 50°S and 50°N, under solar maximum ($F_{10.7}$=200) and geomagnetically quiet conditions. (a): December and January averages, specified by the MSIS; (b): December and January averages, simulated by the WACCM-X; (c): June and July averages, specified by the MSIS; (b): June and July averages, simulated by the WACCM-X.

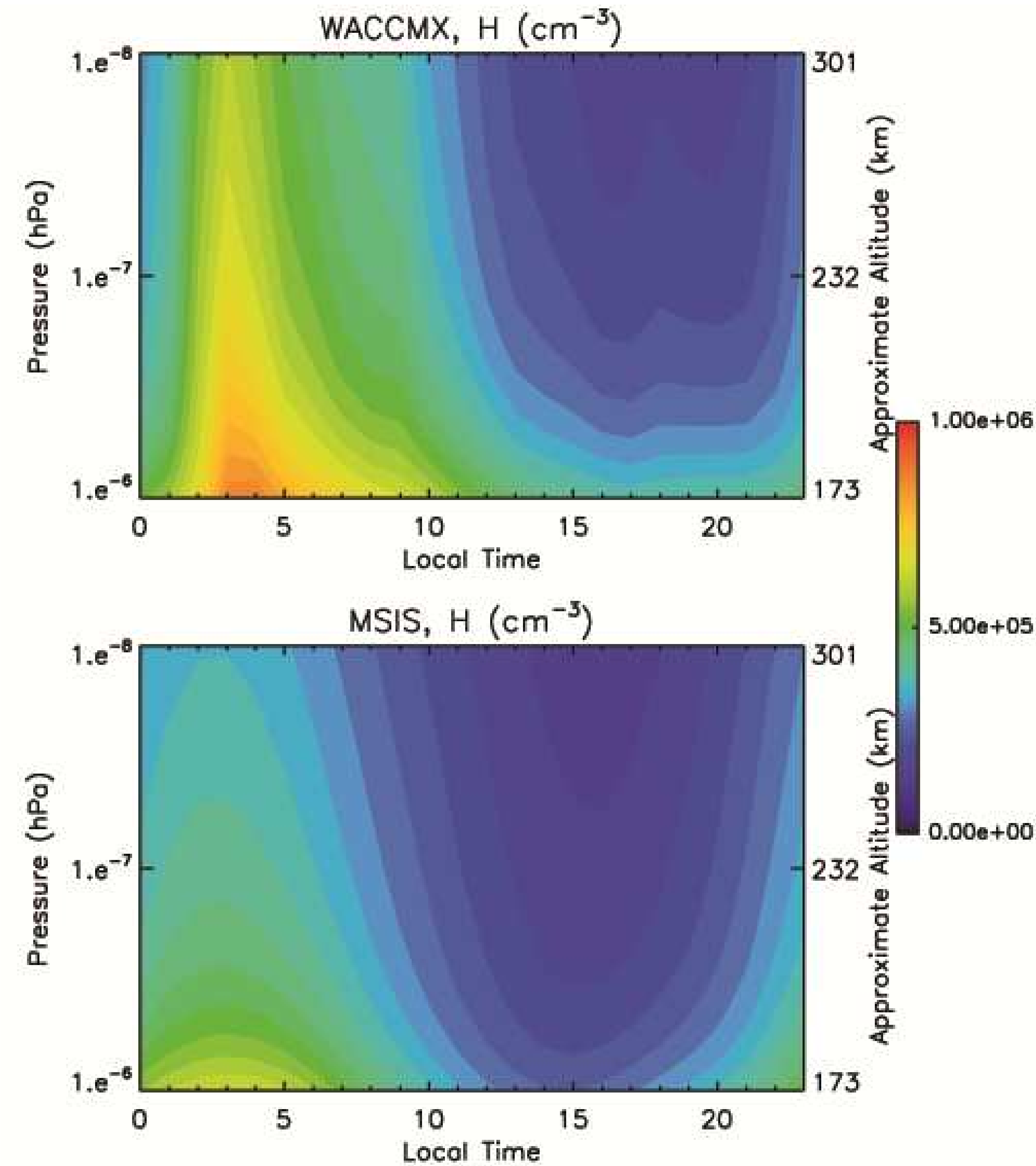

Figure 6: Diurnal variation of hydrogen density on December 1st, under solar minimum and geomagnetically quiet conditions, at (lat=45°S, lon=0°). (a) Simulated by WACCM-X; (b) calculated by MSIS.

Figure 1.

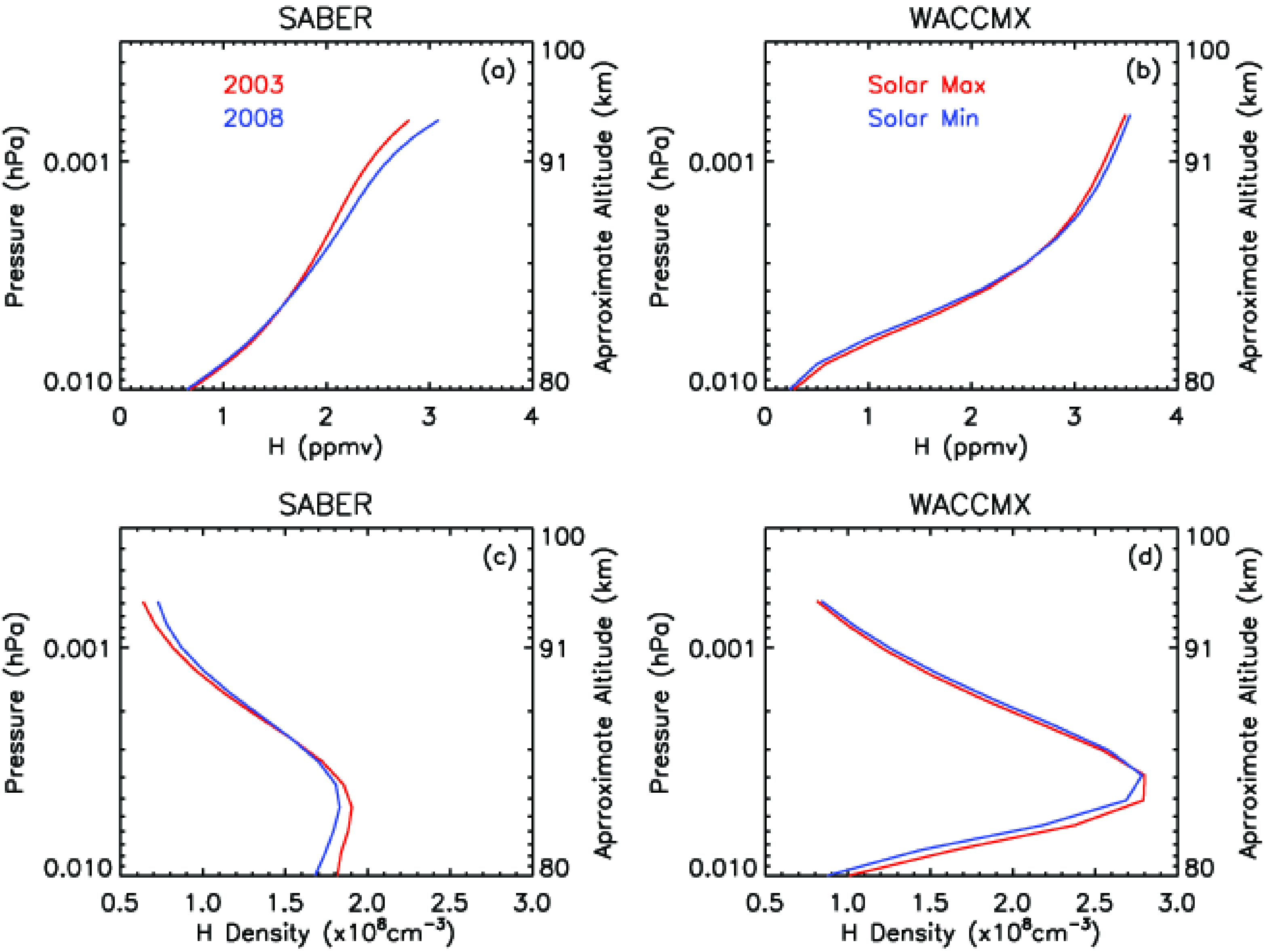
SABER
(a)
2003
2008
Pressure (hPa)
0.001
0.010
100
91
80
Aprroximate Altitude (km)
0
1
2
3
4
H (ppmv)
WACCMX
(b)
Solar Max
Solar Min
Pressure (hPa)
0.001
0.010
100
91
80
Aprroximate Altitude (km)
0
1
2
3
4
H (ppmv)
SABER
(c)
Pressure (hPa)
0.001
0.010
100
91
80
Aprroximate Altitude (km)
0.5
1.0
1.5
2.0
2.5
3.0
H Density (x10^8cm^-3)
WACCMX
(d)
Pressure (hPa)
0.001
0.010
100
91
80
Aprroximate Altitude (km)
0.5
1.0
1.5
2.0
2.5
3.0
H Density (x10^8cm^-3)

Figure 2.

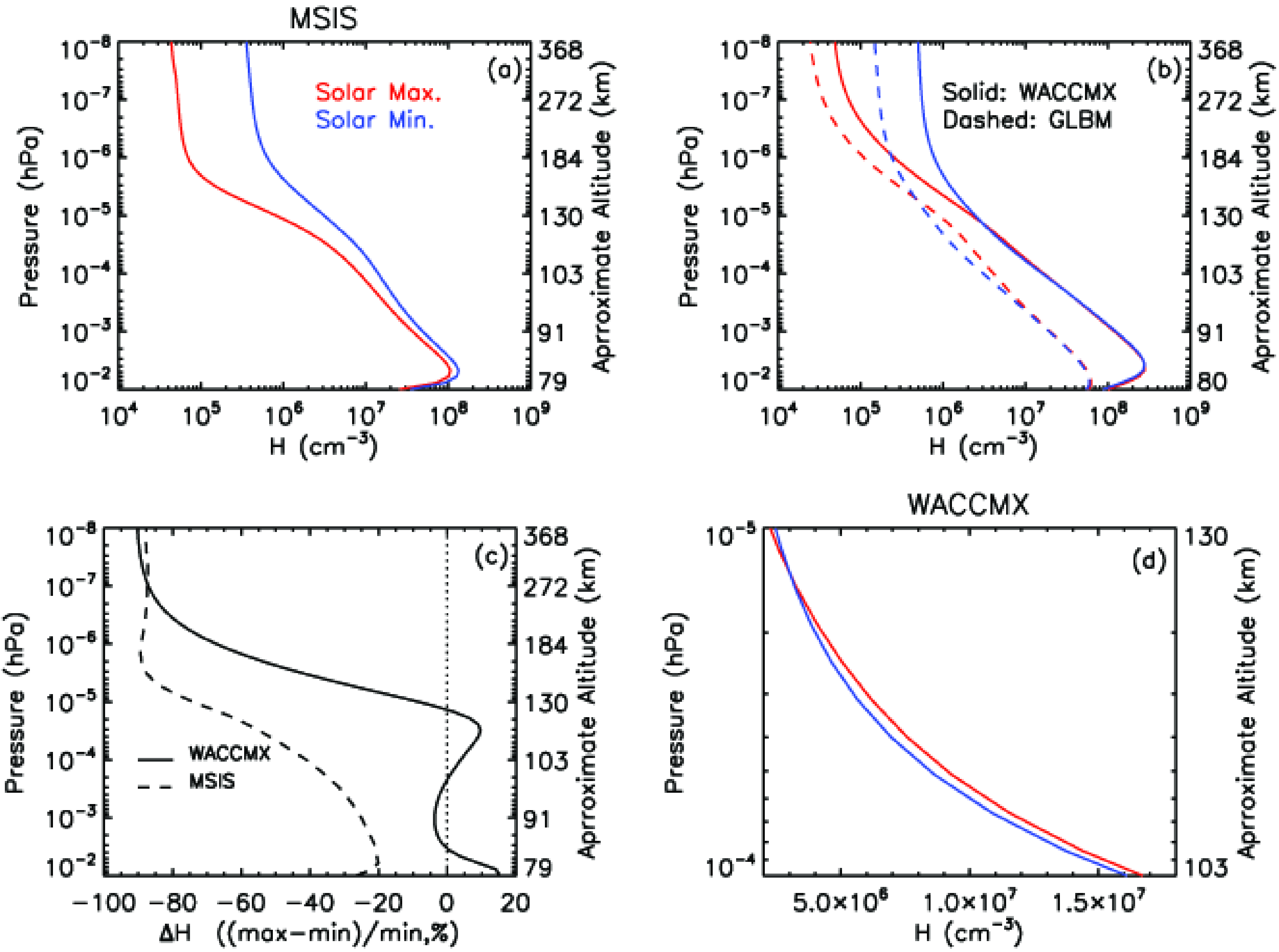

MSIS
(a)
Solar Max.
Solar Min.
Pressure (hPa)
Aprroximate Altitude (km)
H (cm^{-3})
(b)
Solid: WACCMX
Dashed: GLBM
(c)
WACCMX
MSIS
ΔH ((max−min)/min,%)
WACCMX
(d)

Figure 3.

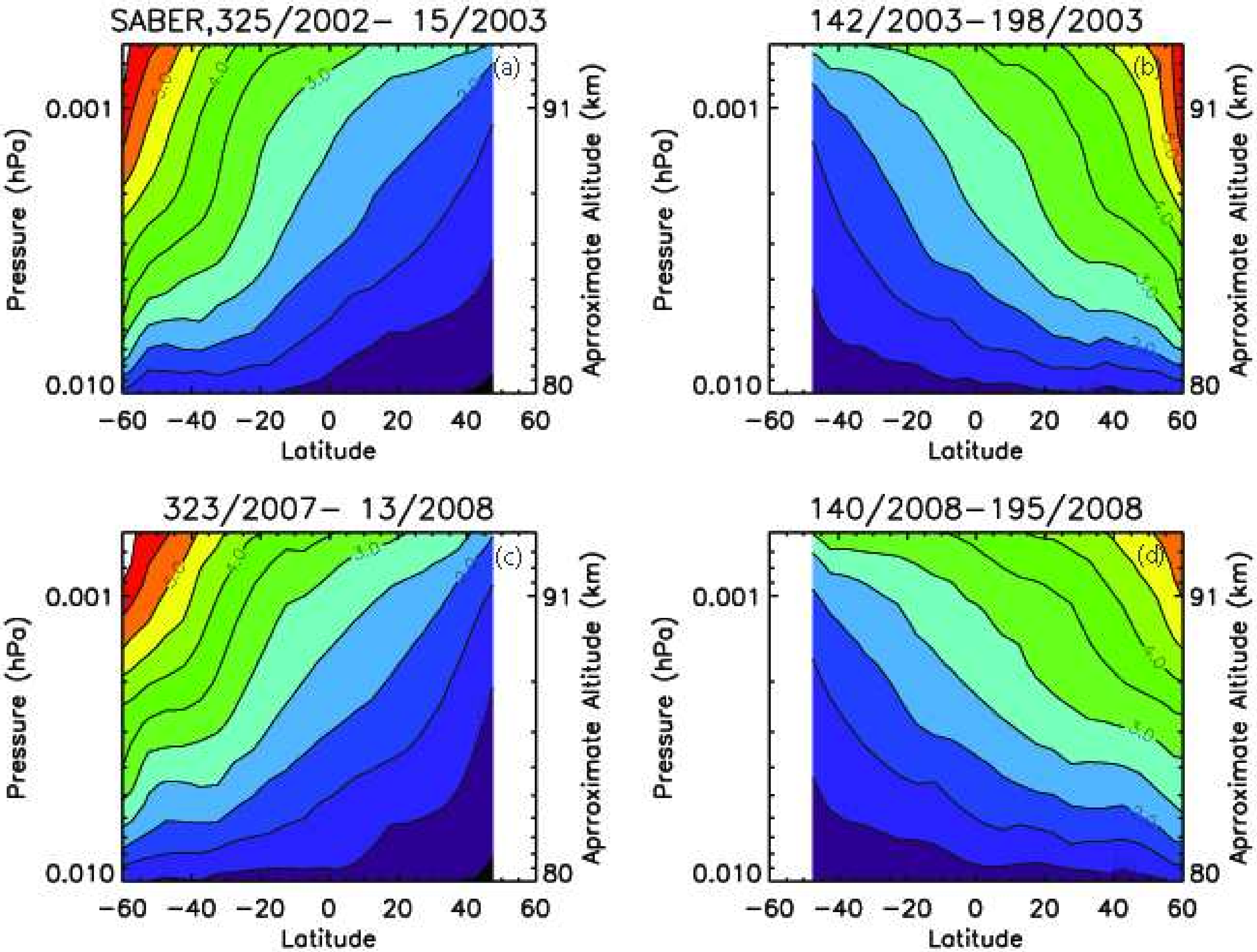

SABER,325/2002- 15/2003
142/2003-198/2003
323/2007- 13/2008
140/2008-195/2008
(a)
(b)
(c)
(d)
Pressure (hPa)
Aprroximate Altitude (km)
Latitude
0.001
0.010
91
80
-60
-40
-20
0
20
40
60

Figure 4.

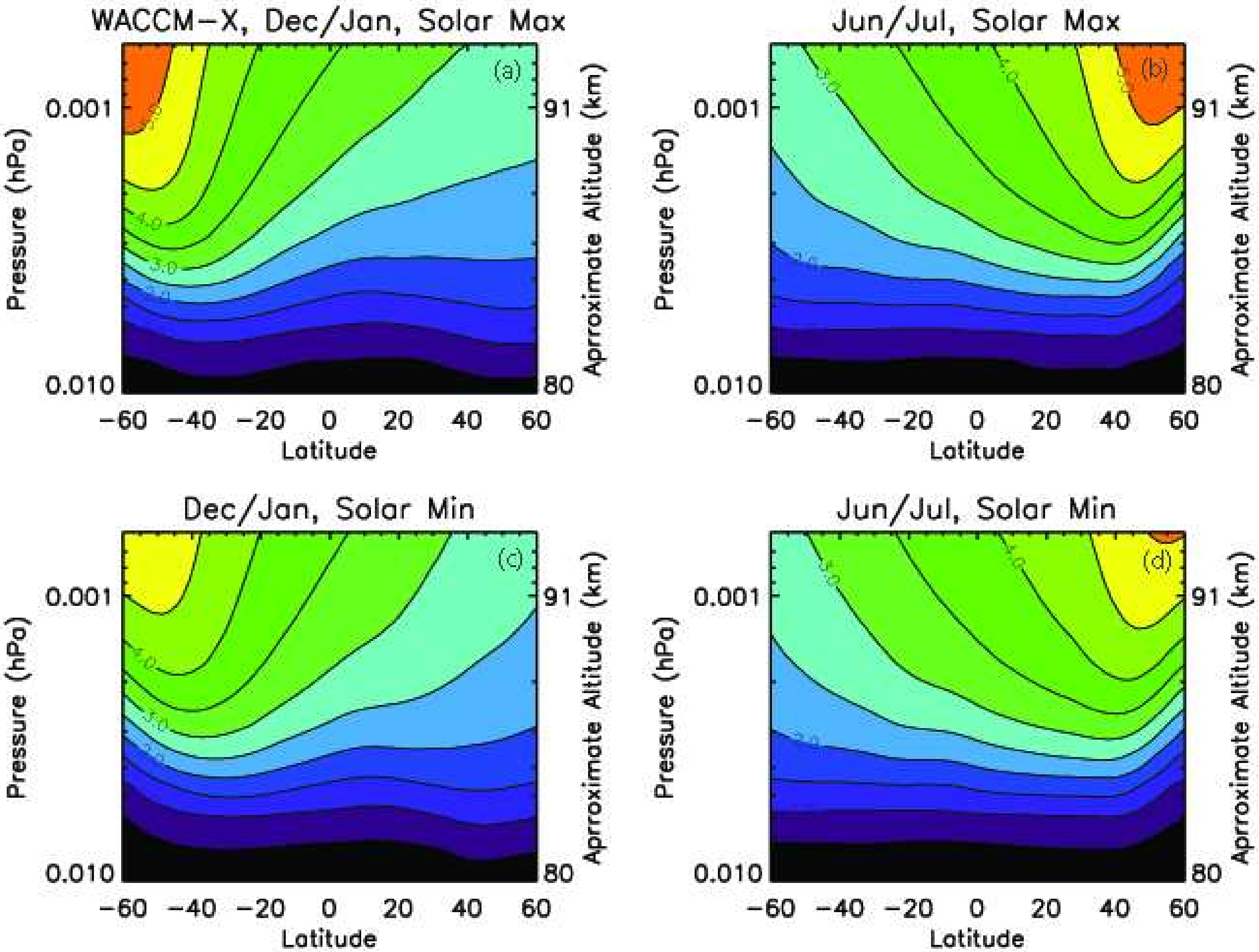
WACCM-X, Dec/Jan, Solar Max
Jun/Jul, Solar Max
Dec/Jan, Solar Min
Jun/Jul, Solar Min
(a)
(b)
(c)
(d)
Pressure (hPa)
Aprroximate Altitude (km)
Latitude
0.001
0.010
91
80
-60
-40
-20
0
20
40
60
4.0
3.0

Figure 5.

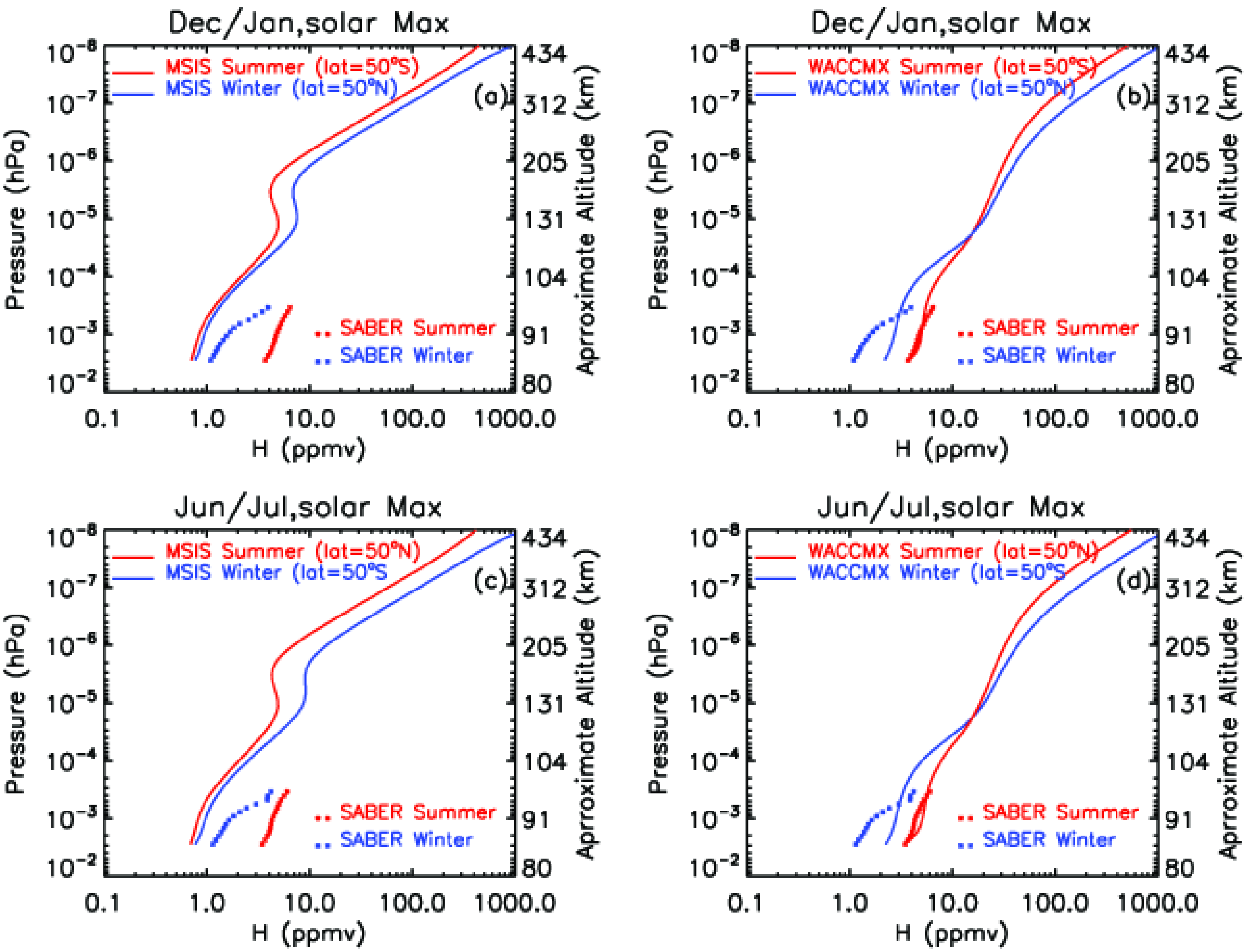
Dec/Jan,solar Max
MSIS Summer (lat=50°S)
MSIS Winter (lat=50°N)
(a)
SABER Summer
SABER Winter
Pressure (hPa)
Aprroximate Altitude (km)
H (ppmv)
Dec/Jan,solar Max
WACCMX Summer (lat=50°S)
WACCMX Winter (lat=50°N)
(b)
SABER Summer
SABER Winter
Jun/Jul,solar Max
MSIS Summer (lat=50°N)
MSIS Winter (lat=50°S)
(c)
SABER Summer
SABER Winter
Jun/Jul,solar Max
WACCMX Summer (lat=50°N)
WACCMX Winter (lat=50°S)
(d)
SABER Summer
SABER Winter

Figure 6.

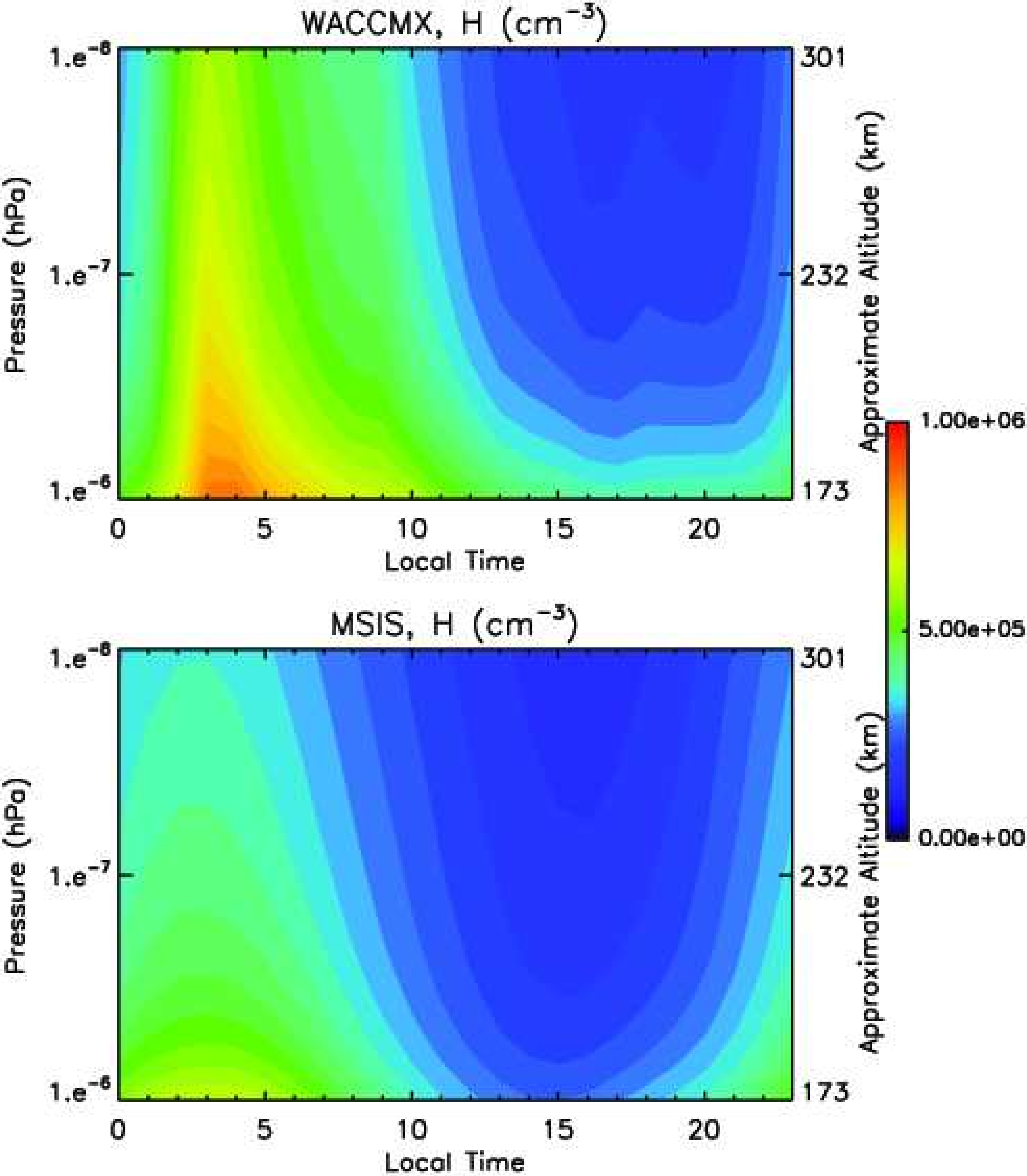
WACCMX, H (cm^{-3})
Pressure (hPa)
Approximate Altitude (km)
1.e-8
1.e-7
1.e-6
301
232
173
0
5
10
15
20
Local Time
MSIS, H (cm^{-3})
1.00e+06
5.00e+05
0.00e+00